Acta Mech 231, 1173–1186 (2020)
https://doi.org/10.1007/s00707-019-02566-w

ORIGINAL PAPER

Qiang Chen · Nicola M. Pugno · Zhiyong Li

The rotation toughening mechanism of barb–barbule joint in the barb delamination of feathers

Received: 1 February 2019 / Revised: 16 August 2019 / Published online: 19 December 2019

Abstract The barb–barbule structure branching from a feather shaft is a basic unit of a bird feather, and the structure is intricately organized to form the feather vane, which plays an important role in keeping the feather's integrity during bird flight. In this paper, by coupling nonlinear large deformations of the barb and barbule, an analytical model of delaminating two neighboring barbs on the basis of critical-friction detaching criteria is developed. Considering the rotation and non-rotation of barb–barbule joints in the delamination, a rotatable model (LargeRM) and a non-rotatable model (LargeNRM) are treated to explain the rotation's contribution to toughening the feather vane. The results show that the predicted interlocking forces of un-detached barbules in the two models were linearly distributed during the delamination. Due to the rotatable barb–barbule joint, the critical detaching force and the elastic strain energy of the two neighboring barbs in the LargeRM are greater than those in the LargeNRM, and this indicates that the rotatable barb–barbule joint could enhance the in-plane delaminating toughness of the feather vane. The present model reveals the nonlinear barb delamination behavior and explains the rotation toughening mechanism of the barb–barbule joint in the barb delamination and further is used to design new bio-inspired interlocking materials, e.g., the feather-inspired Velcro fastener.

Electronic supplementary material The online version of this article (https://doi.org/10.1007/s00707-019-02566-w) contains supplementary material, which is available to authorized users.

Q. Chen (✉) · Z. Li
Biomechanics Laboratory, School of Biological Science and Medical Engineering, Southeast University, Nanjing 210096, P. R. China
E-mail: chenq999@gmail.com

N. M. Pugno
Laboratory of Bio-Inspired and Graphene Nanomechanics, Department of Civil, Environmental and Mechanical Engineering, University of Trento, 38123 Trento, Italy

N. M. Pugno
School of Engineering and Materials Science, Queen Mary University of London, Mile End Road, London E14NS, UK

N. M. Pugno
Ket Lab, Edoardo Amaldi Foundation, Via del Politecnico snc, 00133 Rome, Italy

Z. Li
School of Chemistry, Physics and Mechanical Engineering, Queensland University of Technology (QUT), Brisbane, QLD 4001, Australia

1 Introduction

A feather consists of a shaft with varying cross section from which two rows of barbs branch. The barbs preferentially orientate toward the tip of the feather, and each barb further bifurcates into two rows of barbules called hook and bow barbules. The two types of barbules interlock with each other to form a feather vane through the distributed hooklets on hook barbules, see Fig. 1 [1,2], and this makes the feather vane flexibly deformable. However, literature on the interlocking mechanics of the interesting barb–barbule structure in feathers was not as well reported as other tough natural structures (e.g., nacre [3,4] and beetle's wing [5]). Specifically, the barbule was observed rotating with respect to the barb–barbule joint during the barb delamination (Fig. 1d); in this regard, it is speculated that the rotation may increase the delaminating toughness. Thus, it is necessary to study interlocking mechanics of barb–barbule structure, in particular, the toughening mechanism contributed by the rotatable barb–barbule joint, and further help design a new generation of feather-inspired interlocking structures, e.g., tough Velcro by considering the orientation and rotation of hooks.

From the structure–biomechanical standpoint, there are many studies on feathers. Ennos et al. [6] examined earlier the feather morphology by mechanical tests, and they explained the relationship between the in-plane/out-of-plane mechanical behaviors and the oriented vane formed by barbs and barbules. Moreover, the scaling of feather dimension to body mass of birds was not significantly different, but the feather's flexural stiffness exhibited strong negative allometry; in other words, larger birds have relatively more flexible feathers than smaller birds [7]. The flexibility of feather's in larger birds was further evidenced for the shorter length and narrower feather shaft [8]. This might reduce the stresses on the wing skeleton during takeoff and landing and make feathers less susceptible to mechanical failure [7].

For the feather shaft, it plays an important role in the flexed feather during bird flight [9], and it mainly stores kinetic energy temporarily by bending deformation, and the bending energy is transformed from the wing to the air to lift birds [10]. Thus, the stored energy is determined by the feather's flexural stiffness. Starting from the material view, the shaft is a composite constituting keratin fibers and a protein matrix organized in intricate ways [11]. The measured elastic moduli of the keratin in the shafts of eight species showed weak difference, which hinted that the shaft's flexural stiffness was controlled by its cross-sectional size instead of the keratin properties [10,12]. The geometry-dependent stiffness is consistent with a recent study, which illustrated that the circular-to-square shape change from the feather's proximal to distal end was to maintain the flexural resistance and minimize the weight of the feather [13]. However, some studies reported that the elastic moduli of cortex and medulla in the shaft from the proximal to the distal end varied inversely [14], and the safety factor determined by recording *in vivo* shaft strains in different flying courses of pigeons was more attributed to critical flexural stiffness than to strength [15]. Very recently, the toughening mechanism of the seagull feather shaft was studied, and it was pointed out that the foamy medulla in the shaft prevented

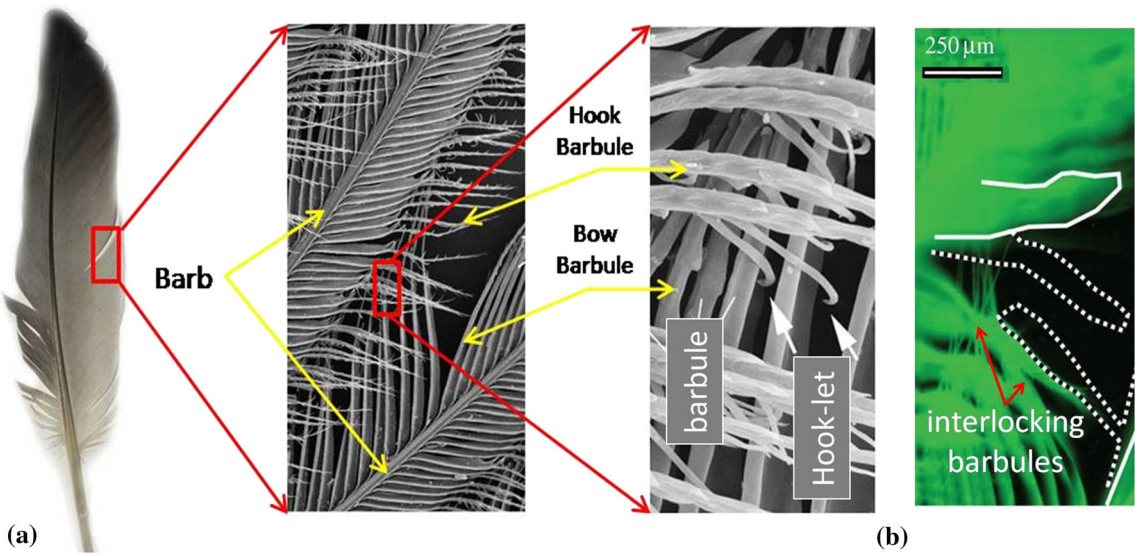

Fig. 1 Barb and two types of barbules in feather [1,2] (**a**), a rotated barbule before (white dash line) and after (white solid line) barb delamination [1] (**b**)

destructive axial cracking and introduced toughening mechanisms, i.e., crack deflection, fiber bridging, and microcracking [16].

Different from the feather shaft, the barb was regarded as the key element of drag reduction mechanism, and its microstructure was examined by a scanning electron microscope [17,18]. The analyses revealed that the barb was a porous-core-filled shell, and the hybrid core-shell structure increased the bending stiffness, buckling resistance, and stability of the feather. Specifically, the feather's flexural stiffness was tested and explained by a foam-filled beam [19].

Regarding the interlocking barbules, Kovalev et al. performed experiments to study self-healing behaviors of barb pairs of a *Cygnus olor* feather and observed that the behaviors were related to the elastic deformation of barbs and the interlocking barbules [1]. Sullivan et al. proposed an interlocking mechanism of the barbs and studied in-plane adhesion and stiffness of barbules, and reported that the interlocking adherence enabled a more robust structure due to minimized barb torsion [18,19]. Recently, basing on beam theories, the authors developed a friction-based hierarchical interlocking barb–barbule model to explain the flaw-tolerant ability in delaminating two barbs [2]. Although these studies have revealed its interlocking adherent robust and flaw-tolerant mechanisms of the barb–barbule structure, they did not discuss the rotation of the barb–barbule joint in the barb delamination process.

To this end, this work aims to explain the contribution of the rotatable barb–barbule joint to the tough feather vane. A fundamental large deformation theory of a rotatable cantilever beam is first developed. Then, the solution of the theory is applied to treat the large deformations of barb and barbule, respectively. To explain the toughening mechanism of the rotatable barb–barbule joint in the delamination of two neighboring barbs, a rotatable model (LargeRM) and a non-rotatable model (LargeNRM) are discussed. Finally, comparison of dimensionless elastic strain energies of the two models shows the superiority of the LargeRM's toughness.

2 Large deformation theory of a rotatable cantilever beam

In the delamination of two neighboring barbs, interlocking barbules were observed to deform elastically and rotate at the barb–barbule joint (Fig. 1d). Accordingly, the barbule is modeled as a rotatable cantilever with respect to the barb and the barb as a non-rotatable one with respect to feather shaft. Here, the rotatable cantilever is composed of a hinged beam at the end O and an angular spring (Fig. 2). The non-rotatable is a specific case of the rotatable cantilever when the rotation stiffness of the angular spring is infinite. Then, for the rotatable cantilever, when it is subjected to a force F acting on its free end, it deforms and rotates synchronously with respect to the end O. A force analysis gives a moment equilibrium equation of an arbitrary point $P(x, y)$:

$$D\frac{\mathrm{d}\theta}{\mathrm{d}s} = F\cos\varphi\,(l\cos\alpha_0 + \delta_x - x) + F\sin\varphi\left(l\sin\alpha_0 + \delta_y - y\right), \tag{1}$$

where D is the bending rigidity of the cantilever, θ and s are angular and curvilinear coordinates of the arbitrary point P, φ is an included angle made by the force direction and positive y-axis, l is the beam length, α_0 is an initial included angle made by the un-deformed cantilever (dash line in Fig. 2a) and positive x-axis, δ_x and δ_y are displacements of the free end in the x- and y-directions, respectively. Here, φ is defined to be positive if the force direction is clockwise with respect to the positive y-axis, otherwise, it is negative; in particular, φ is 0 if the force direction is parallel to the positive y-axis and goes through the filled circle (Fig. 2b). θ is defined to be positive if the tangent at the point P pointing at the free end is clockwise with respect to the positive x-axis (Fig. 2a), otherwise, it is negative.

Setting the following dimensionless quantities $K = l\sqrt{F/D}$, $\bar{s} = s/l$, $\bar{\delta}_x = \delta_x/l$, $\bar{\delta}_y = \delta_y/l$, $\bar{x} = x/l$, $\bar{y} = y/l$, Eq. (1) is rewritten as

$$\frac{\mathrm{d}\theta}{\mathrm{d}\bar{s}} = K^2\cos\varphi\left(\cos\alpha_0 + \bar{\delta}_x - \bar{x}\right) + K^2\sin\varphi\left(\sin\alpha_0 + \bar{\delta}_y - \bar{y}\right). \tag{2}$$

Deriving Eq. (2) and employing $\mathrm{d}\bar{x}/\mathrm{d}\bar{s} = \cos\theta$ and $\mathrm{d}\bar{y}/\mathrm{d}\bar{s} = \sin\theta$, we obtain

$$\frac{\mathrm{d}^2\theta}{\mathrm{d}\bar{s}^2} = -K^2\cos\left(\theta - \varphi\right), \tag{3}$$

which is solved as

$$\left(\frac{\mathrm{d}\theta}{\mathrm{d}\bar{s}}\right)^2 = -2K^2\sin\left(\theta - \varphi\right) + C. \tag{4}$$

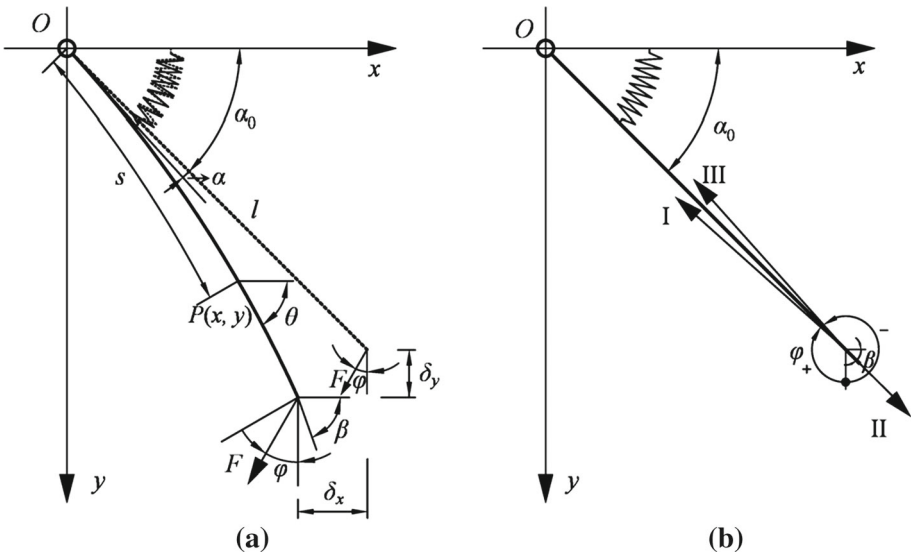

Fig. 2 A rotatable cantilever. **a** Force analysis, **b** Sign convention of φ

The boundary condition at the free end satisfies $\mathrm{d}\theta/\mathrm{d}\bar{s}|_{\theta=\beta} = 0$, where β is the angular coordinate of the free end. Then, the curvature of the deformed cantilever is expressed as

$$\frac{\mathrm{d}\theta}{\mathrm{d}\bar{s}} = \pm\sqrt{2}K\sqrt{\sin(\beta-\varphi) - \sin(\theta-\varphi)}. \tag{5}$$

As for the sign of the curvature expression (5), two extreme states (I and III) and an intermediate one (II) are analyzed; see Fig. 2b. When the cantilever is between states I and II (i.e., $-\pi/2 < \beta - \varphi < \pi/2$), $\mathrm{d}\theta/\mathrm{d}\bar{s} > 0$, whereas when it is between states II and III (i.e., $\pi/2 < \beta - \varphi < 3\pi/2$), $\mathrm{d}\theta/\mathrm{d}\bar{s} < 0$. Rearranging Eq. (5) and employing the transformation of trigonometric functions leads to a differential equation of the curvilinear coordinate of the cantilever beam:

$$\mathrm{d}\bar{s} = \pm\frac{p}{K}\frac{\mathrm{d}\left(\frac{\theta-\varphi}{2}+\frac{\pi}{4}\right)}{\sqrt{1-p^2\sin^2\left(\frac{\theta-\varphi}{2}+\frac{\pi}{4}\right)}}, \tag{6}$$

where $p^2 = 2/[1+\sin(\beta-\varphi)]$. Due to the beam rotation, θ varies from $\alpha_0+\alpha$ to β. Integrating Eq. (6), the curvilinear coordinate $\bar{s}(\theta)$ of the arbitrary point P is expressed as

$$\bar{s}(\theta) = \pm\frac{p}{K}\left[F\left(p, \frac{\theta-\varphi}{2}+\frac{\pi}{4}\right) - F\left(p, \frac{\alpha_0+\alpha-\varphi}{2}+\frac{\pi}{4}\right)\right], \tag{7}$$

where the function $F(p,\xi)$ with a general amplitude ξ is the incomplete elliptical integration of the first kind. If the cantilever is considered to be an elastic, i.e., $\bar{s}(\beta) = 1$, we have

$$K = \pm p\left[F\left(p, \frac{\beta-\varphi}{2}+\frac{\pi}{4}\right) - F\left(p, \frac{\alpha_0+\alpha-\varphi}{2}+\frac{\pi}{4}\right)\right]. \tag{8}$$

Invoking Eq. (5), the Cartesian coordinates of the point P can be obtained by integrating $\mathrm{d}\bar{x} = \cos\theta\ \mathrm{d}\bar{s}$ and $\mathrm{d}\bar{y} = \sin\theta\ \mathrm{d}\bar{s}$. Substituting θ with $(\theta-\varphi+\varphi)$ in $\mathrm{d}\bar{x}$ and $\mathrm{d}\bar{y}$, the Cartesian coordinates of the point P are expressed as

$$\begin{pmatrix}\bar{x}(\theta)\\ \bar{y}(\theta)\end{pmatrix} = \pm\frac{1}{\sqrt{2}K}\begin{pmatrix}\cos\varphi & -\sin\varphi\\ \sin\varphi & \cos\varphi\end{pmatrix}\begin{pmatrix}A(\theta)\\ B(\theta)\end{pmatrix} \tag{9}$$

with

$$
\begin{aligned}
A(\theta) &= \int_{\alpha_0+\alpha}^{\theta} \frac{\cos(\theta-\varphi)}{\sqrt{\sin(\beta-\varphi)-\sin(\theta-\varphi)}}\mathrm{d}\theta \\
&= 2\left(\sqrt{\sin(\beta-\varphi)-\sin(\alpha_0+\alpha-\varphi)}-\sqrt{\sin(\beta-\varphi)-\sin(\theta-\varphi)}\right), \\
B(\theta) &= \int_{\alpha_0+\alpha}^{\theta} \frac{\sin(\theta-\varphi)}{\sqrt{\sin(\beta-\varphi)-\sin(\theta-\varphi)}}\mathrm{d}\theta \\
&= \sqrt{2}p\left[\sin(\beta-\varphi)\left(F\left(p,\frac{\theta-\varphi}{2}+\frac{\pi}{4}\right)-F\left(p,\frac{\alpha_0+\alpha-\varphi}{2}+\frac{\pi}{4}\right)\right)\right. \\
&\quad \left.-\frac{2}{p^2}\left(E\left(p,\frac{\theta-\varphi}{2}+\frac{\pi}{4}\right)-E\left(p,\frac{\alpha_0+\alpha-\varphi}{2}+\frac{\pi}{4}\right)\right)\right],
\end{aligned}
$$

where the function $E(p,\xi)$ with a general amplitude ξ is the incomplete elliptical integration of the second kind. Moreover, considering the moment equilibrium of the cantilever with respect to the end O, the following equation arrives:

$$
\lambda\alpha = F\cos\varphi\, x(\beta) + F\sin\varphi\, y(\beta) = \pm\frac{Fl}{\sqrt{2}K}A(\beta), \tag{10}
$$

where λ is the rotation stiffness of the angular spring which has the physical unit N · m/rad. Rearranging Eq. (10) leads to a new expression as

$$
K = \pm\frac{\bar{\lambda}\alpha}{\sqrt{2\left[\sin(\beta-\varphi)-\sin(\alpha_0+\alpha-\varphi)\right]}}, \tag{11}
$$

where $\bar{\lambda}=\lambda l/D$ is a new dimensionless parameter indicating the cantilever's deformability, i.e., the relative relationship between the rotation and bending abilities. When $\bar{\lambda}\to 0$, the cantilever is an indeterminate structure with one end hinged; in contrast, if $\bar{\lambda}\to\infty$, it is the non-rotatable cantilever. The reasonability of the theory is illustrated by calculating $\bar{\delta}_x$ and $\bar{\delta}_y$ under different K, α_0, and $\bar{\lambda}$ in the Supporting Material.

3 Delamination theory of two neighboring barbs

In feathers, a single hook barbule always carries several hooklets at its end, and the ith hook barbule may simultaneously interact with the ith, $(i+1)$th, or more bow barbules (the third figure in Fig. 1a). Plus, the branched hook and bow barbules are not strictly symmetrical (the second figure in Fig. 1a). Here, two simplifications are made (Fig. 3a): (1) The ith hook barbule only interacts with the ith bow barbule at one point; (2) the hook and bow barbules are distributed symmetrically, i.e., the initial angles α_0 made by the barbules and barbs are equal. In Fig. 3a, the barb and barbule are represented by thick and thin lines, respectively.

In the model, both barb and barbule are treated as large-deformation beams to which the solution in Sect. 2 is applicable. The total number of pairs of hook and bow barbules is n, and the number of pairs of interlocking hook and bow barbules is k (e.g., $n=9$, and $k=3$ in Fig. 3a). This means that the kth pair of barbules carries the greatest interlocking force among all interlocking barbules due to its greatest elastic deformation. Addressing the state, three coordinate systems are introduced: One is global (X, Y) for the deformed barbs indicated by superscript (1) (Fig. 3a), and the local (x, y) and auxiliary one (x', y') are for the deformed barbules indicated by superscript (2) (Fig. 3b). The auxiliary (x', y') is introduced for the coordinate transformation from local (x, y) to global coordinates (X, Y). Thanks to the structural symmetry about the axis X, we study the half structure of the ith $(1<i\le k)$ interlocking barbule; see Fig. 3b.

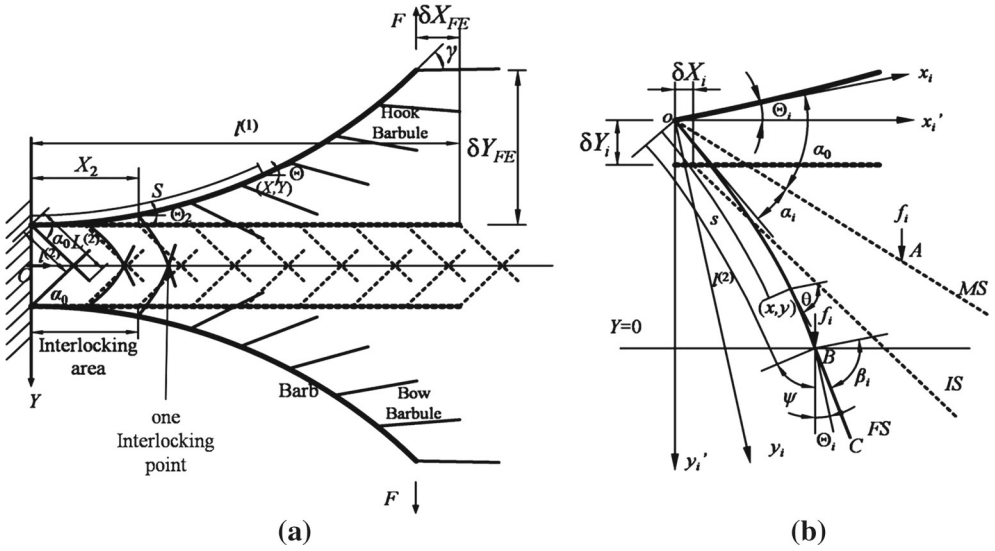

Fig. 3 Simplified delamination model of two neighboring barbs (barbs in thick lines and barbules in thin lines). **a** Before- (dash lines) and after-delaminated (solid lines) structures; **b** Force analysis of the semi-structure of ith pair of interlocking barbules

3.1 Large deformation of barb

In the delamination, the barb is regarded as a classical cantilever with one end fixed. Here, different from the literature [2] where the barb was modeled as a small-deformation beam, the barb here is treated as a large-deformation beam. Considering the coupling deformations of the barb and barbule, for an arbitrary point (X, Y) of the barb locating between the ith and (i + 1)th interlocking barbules, the moment equilibrium at the arbitrary point is expressed as

$$D^{(1)}\frac{\mathrm{d}\Theta}{\mathrm{d}S} = F\left(l^{(1)} + \delta X_{FE} - X\right) - \sum_{j=i+1}^{k} f_j\left(X_{B,j} - X\right), \tag{12}$$

where $D^{(1)}$ is the bending rigidity of the barb, $l^{(1)}$ is the barb length, F is the external detaching force at the free end of the barb, δX_{FE} is the horizontal displacement of the free end of the barb, f_j is the interlocking force at the point A of the jth barbule to that in the FS state (Fig. 3b), and $X_{B,j}$ is the coordinate of the interlocking point B of the jth barbule in the global system. Defining a set of dimensionless quantities $K^{(1)} = l^{(1)}\sqrt{F/D^{(1)}}$, $K_j^{(2)} = l^{(2)}\sqrt{f_j/D^{(2)}}$, $\bar{S} = S/l^{(1)}$, $\delta\bar{X}_{FE} = \delta X_{FE}/l^{(1)}$, $\bar{X} = X/l^{(1)}$, $\bar{X}_{B,j} = X_{B,j}/l^{(1)}$, Eq. (12) is re-expressed as

$$\frac{\mathrm{d}\Theta}{\mathrm{d}\bar{S}} = \left(K^{(1)}\right)^2\left(1 + \delta\bar{X}_{FE} - \bar{X}\right) - \frac{D^{(2)}/\left(l^{(2)}\right)^2}{D^{(1)}/\left(l^{(1)}\right)^2}\sum_{j=i+1}^{k}\left(K_j^{(2)}\right)^2\left(\bar{X}_{B,j} - \bar{X}\right), \tag{13}$$

where $D^{(2)}$ is the bending rigidity of the barbule and $l^{(2)}$ is the deformed length of the barbule. From Eq. (13), it is readily seen that the influence of the barbules on the barb is negligible if $D^{(2)}/(l^{(2)})^2 << D^{(1)}/(l^{(1)})^2$, but the influence of the barb on the barbule, i.e., the translation and rotation of the end o caused by the deformed barb in Fig. 3b, must be taken into account. With the negligible influence of the barbule on the barb, the problem here shrinks to a specific case of the cantilever in Sect. 2, and the upper barb cantilever in Fig. 3a provides $\alpha_0^{\mathrm{barb}} = 0$, $\alpha^{\mathrm{barb}} = 0$, $\varphi^{\mathrm{barb}} = -\pi$, $\beta = \gamma$. It is worth mentioning that according to the sign convention of θ in Eq. (1), γ is negative in the global system. Then, substituting the four angular parameters into Eq. (7), the dimensionless curvilinear coordinate of the barb is

$$\bar{S}(\Theta) = -\frac{P}{K^{(1)}}\left[F\left(P, \frac{3\pi}{4} + \frac{\Theta}{2}\right) - F\left(P, \frac{3\pi}{4}\right)\right], \tag{14}$$

where $P^2 = 2/(1-\sin\gamma)$, and the inextensible condition $\bar{S}(\gamma) = 1$ provides

$$K^{(1)} = -P\left[F\left(P, \frac{3\pi}{4} + \frac{\gamma}{2}\right) - F\left(P, \frac{3\pi}{4}\right)\right]. \tag{15}$$

With given dimensionless force $K^{(1)}$, the rotation angle γ of the free end is solved. Correspondingly, the barb profile can be described by referring to Eq. (9):

$$\bar{X}(\Theta) = \frac{\sqrt{2}}{K^{(1)}}\left(\sqrt{-\sin\gamma} - \sqrt{-\sin\gamma + \sin\Theta}\right), \tag{16a}$$

$$\begin{aligned}\bar{Y}(\Theta) = &-\left(\frac{l^{(2)}}{l^{(1)}}\right)\sin\alpha_0^{\text{barbule}} + \frac{P}{K^{(1)}}\left[\sin\gamma\left(F\left(P, \frac{3\pi}{4}\right) - F\left(P, \frac{3\pi}{4} + \frac{\Theta}{2}\right)\right)\right.\\ &\left.+\frac{2}{P^2}\left(E\left(P, \frac{3\pi}{4}\right) - E\left(P, \frac{3\pi}{4} + \frac{\Theta}{2}\right)\right)\right].\end{aligned} \tag{16b}$$

For the ith interlocking barbule, its curvilinear coordinate at the ith barb–barbule joint satisfies $\bar{S}(\Theta_i) = \frac{i-1}{n-1}$, and substituting $\bar{S}(\Theta_i)$ into Eq. (14), Θ_i is calculated. Then, the displacements of the ith barb–barbule joint in the X- and Y-directions are expressed as

$$\delta\bar{X}_i = \frac{\sqrt{2}}{K^{(1)}}\left(\sqrt{-\sin\gamma} - \sqrt{-\sin\gamma + \sin\Theta_i}\right) - \frac{i-1}{n-1}, \tag{17a}$$

$$\begin{aligned}\delta\bar{Y}_i = &\frac{P}{K^{(1)}}\left[\sin\gamma\left(F\left(P, \frac{3\pi}{4}\right) - F\left(P, \frac{3\pi}{4} + \frac{\Theta_i}{2}\right)\right)\right.\\ &\left.+\frac{2}{P^2}\left(E\left(P, \frac{3\pi}{4}\right) - E\left(P, \frac{3\pi}{4} + \frac{\Theta_i}{2}\right)\right)\right].\end{aligned} \tag{17b}$$

The solved parameters Θ_i, $\delta\bar{X}_i$, and $\delta\bar{Y}_i$ are negative and represent the influence of the barb on the barbule, and they will be included in the deformation of the barbules.

3.2 Large deformation of barbule

Considering the internal interlocking force of the hook and bow barbules in the neighboring barbs as an external force applied on barbule, the large deformation of the barbule is also calculated by the solution in Sect. 2. It is worth mentioning that here to explain the toughening mechanism of the rotatable barb–barbule joint, two sub-models are treated: One includes the joint rotation (LargeRM), and the other excludes the joint rotation (LargeNRM).

3.2.1 LargeRM: Delamination with rotatable barbule

The large deformation of the barbule in the delamination is decomposed into two steps: The first is caused by the barb, which translates the barbule by $-\delta\bar{X}_i$, $-\delta\bar{Y}_i$ and rotates it by-Θ_i with respect to its initial position, i.e., from the state *IS* to the state *MS*; see Fig. 3b. The second is caused by the interlocking force f_i at the point A, which deforms the barbule from the *MS* state to the *FS* state, and the point A is relocated at the point B. Moreover, the included angle between the barb and barbule is changed into $\alpha_0 + \alpha_i$, where α_i is the rotation angle of the ith barbule. Here, the critical-friction-based criteria is used to judge the detachment of interlocking barbules, namely interlocking barbules detach immediately when the critical friction angle ψ_{frict} is reached. Then, the detaching criterion requires that the angular coordinate β_i at the interlocking point B satisfies $\beta_i - (-\Theta_i) = \psi > \psi_{frict}$. In the local system (x, y), replacing φ, α, and β in Eqs. (8) and (11) with $-\Theta_i$, α_i, and β_i, we obtain:

$$K_i^{(2)} = p_i\left[F\left(p_i, \frac{\beta_i + \Theta_i}{2} + \frac{\pi}{4}\right) - F\left(p_i, \frac{\alpha_0^{\text{barbule}} + \alpha_i + \Theta_i}{2} + \frac{\pi}{4}\right)\right], \tag{18}$$

$$K_i^{(2)} = \frac{\Lambda \alpha_i}{\sqrt{2\left[\sin\left(\beta_i + \Theta_i\right) - \sin\left(\alpha_0^{\text{barbule}} + \alpha_i + \Theta_i\right)\right]}}, \tag{19}$$

where $p_i^2 = 2/[1 + \sin(\beta_i + \Theta_i)]$ and the two equations included three unknown parameters α_i, β_i, and $K_i^{(2)}$. It is noted that for the barbule, $\mathrm{d}\theta/\mathrm{d}\bar{s} > 0$; thus, Eqs. (18) and (19) are positive. The coordinates $(\bar{x}_i^{oB}, \bar{y}_i^{oB})$ of the deformed oB part of the barbules in the local coordinate system (x, y) are calculated from Eq. (9):

$$\begin{pmatrix} \bar{x}_i^{oB}(\theta) \\ \bar{y}_i^{oB}(\theta) \end{pmatrix} = \frac{1}{\sqrt{2}K_i^{(2)}} \begin{pmatrix} \cos\Theta_i & \sin\Theta_i \\ -\sin\Theta_i & \cos\Theta_i \end{pmatrix} \begin{pmatrix} A(\theta) \\ B(\theta) \end{pmatrix}. \tag{20}$$

Transforming the coordinates of the deformed oB part into the global coordinate system (X, Y), the global coordinates are obtained as

$$\begin{aligned} \begin{pmatrix} \bar{X}_i^{oB}(\theta) \\ \bar{Y}_i^{oB}(\theta) \end{pmatrix} &= \begin{pmatrix} l^{(1)}/l^{(2)} \end{pmatrix} \begin{pmatrix} \bar{X}_i \\ \bar{Y}_i \end{pmatrix} + \begin{pmatrix} \cos\Theta_i & -\sin\Theta_i \\ \sin\Theta_i & \cos\Theta_i \end{pmatrix} \begin{pmatrix} \bar{x}_i^{oB}(\theta) \\ \bar{y}_i^{oB}(\theta) \end{pmatrix} \\ &= \begin{pmatrix} l^{(1)}/l^{(2)} \end{pmatrix} \begin{pmatrix} \bar{X}_i \\ \bar{Y}_i \end{pmatrix} + \frac{1}{\sqrt{2}K_i^{(2)}} \begin{pmatrix} A(\theta) \\ B(\theta) \end{pmatrix}, \end{aligned} \tag{21}$$

where $\bar{X}_i^{oB}(\theta) = X_i^{oB}(\theta)/l^{(2)}$ and $\bar{Y}_i^{oB}(\theta) = Y_i^{oB}(\theta)/l^{(2)}$. In particular, the coordinates of the point B of the ith barbule are obtained from Eq. (21):

$$\begin{pmatrix} \bar{X}_i^{oB}(\beta_i) \\ \bar{Y}_i^{oB}(\beta_i) \end{pmatrix} = \begin{pmatrix} l^{(1)}/l^{(2)} \end{pmatrix} \begin{pmatrix} \bar{X}_i \\ \bar{Y}_i \end{pmatrix} + \frac{1}{\sqrt{2}K_i^{(2)}} \begin{pmatrix} A(\beta_i) \\ B(\beta_i) \end{pmatrix}, \tag{22}$$

where

$$\begin{aligned} A(\beta_i) &= 2\left(\sqrt{\sin\left(\beta_i + \Theta_i\right) - \sin\left(\alpha_0^{\text{barbule}} + \alpha_i + \Theta_i\right)}\right), \\ B(\beta_i) &= \sqrt{2}p_i \left[\sin\left(\beta_i + \Theta_i\right)\left(F\left(p_i, \frac{\beta_i + \Theta_i}{2} + \frac{\pi}{4}\right) - F\left(p_i, \frac{\alpha_0^{\text{barbule}} + \alpha_i + \Theta_i}{2} + \frac{\pi}{4}\right)\right),\right. \\ &\quad \left. -\frac{2}{p_i^2}\left(E\left(p_i, \frac{\beta_i + \Theta_i}{2} + \frac{\pi}{4}\right) - E\left(p_i, \frac{\alpha_0^{\text{barbule}} + \alpha_i + \Theta_i}{2} + \frac{\pi}{4}\right)\right)\right]. \end{aligned}$$

Because of the symmetry, the Y coordinate satisfies $\bar{Y}_i^{oB}(\beta_i) = 0$; then, we have

$$K_i^{(2)} = \frac{B(\beta_i)}{\sqrt{2}\left[\sin\alpha_0^{\text{barbule}} - \delta\bar{Y}_i\left(l^{(1)}/l^{(2)}\right)\right]}. \tag{23}$$

In Eq. (23), there are also three unknown parameters α_i, β_i, and $K_i^{(2)}$. Thus, substituting Eq. (23) into Eqs. (18) and (19), we obtain an equation system with two unknown parameters, α_i and β_i. With the solution of α_i and β_i, the dimensionless force $K_i^{(2)}$ in each barbule can be calculated. For the un-deformed part BC in the barbules, it satisfies

$$\bar{Y}_i^{BC} = \tan\left(\beta_i + \Theta_i\right)\left(\bar{X}_i^{BC} - \bar{X}_i^{oB}(\beta_i)\right), \tag{24}$$

where $\bar{Y}_i^{BC} = Y_i^{BC}/l^{(2)}$, $\bar{X}_i^{BC} = X_i^{BC}/l^{(2)}$ is from $\bar{X}_i^{oB}(\beta_i)$ to $\bar{X}_i^{oB}(\beta_i) + \left(L^{(2)}/l^{(2)} - 1\right)\cos\left(\beta_i + \Theta_i\right)$, and $L^{(2)}$ is the total length of the barbule.

Equations (18–24) are derived for the interlocking barbules, whereas, for the *detached barbules* $(k + 1 \le i \le n)$, the coordinate of the barbule is derived as

$$\bar{Y}_i^{oC} = \tan\left(\alpha_0^{\text{barbule}} + \Theta_i\right)\left(\bar{X}_i^{oC} - \bar{X}_i\left(\frac{l^{(1)}}{l^{(2)}}\right)\right) + \bar{Y}_i\left(\frac{l^{(1)}}{l^{(2)}}\right), \tag{25}$$

where $\bar{Y}_i^{oC} = Y_i^{oC}/l^{(2)}, \bar{X}_i^{oC} = X_i^{oC}/l^{(2)}$ is from $\bar{X}_i\left(l^{(1)}/l^{(2)}\right)$ to $\bar{X}_i\left(l^{(1)}/l^{(2)}\right)+\left(L^{(2)}/l^{(2)}\right)\cos\left(\alpha_0^{\text{barbule}}+\Theta_i\right)$.

3.2.2 LargeNRM: Delamination with non-rotatable barbule

In the LargeNRM model, the barbules do not rotate at the barb–barbule joint in the delamination, *i.e.*, $\alpha_i = 0$; then, the model is a specific case of the LargeRM. It is worth mentioning that Eq. (19) is not available because $K_i^{(2)} = 0$ always holds; obviously, this is not true. Then, substituting $\alpha_i = 0$ into Eqs. (18) and (23), they give β_i and $K_i^{(2)}$.

4 Elastic strain energy stored in the delaminating barbs

Feather shaft plays an important role in transforming the kinetic energy to bending deformation energy and then transforms the bending energy from the wing to the air [10]. The deformations of the barb and barbule also store the kinetic energy, and they guarantee the flexibility and integrity of the feather vane. In the sense of the energy, a better structure could store more energy without (or with less) structural failure. Then, to answer the question why the barb–barbule joint is rotatable, we compared the elastic strain energy of the rotatable and non-rotatable models. The LargeRM includes three components (barb, barbule, and angular spring). The LargeNRM includes two components (barb and barbule) due to the non-rotation of the barbule. Then, the total elastic strain energies in the two types of models are expressed as

$$U_{\text{LargeRM}}^k = U_{\text{barb}} + \sum_1^k \left(U_{\text{barbule}}^i + U_{\text{spring}}^i\right), \tag{26}$$

$$U_{\text{LargeNRM}}^k = U_{\text{barb}} + \sum_1^k U_{\text{barbule}}^i, \tag{27}$$

where the elastic strain energies of the barb, barbule, and angular spring are, respectively, calculated:

$$\begin{aligned}
U_{\text{barb}} &= \frac{1}{2}\frac{D^{(1)}}{l^{(1)}}\int_0^1 \left(\frac{\mathrm{d}\Theta}{\mathrm{d}\bar{S}}\right)^2 \mathrm{d}\bar{S} = 2\frac{D^{(1)}}{l^{(1)}}\cdot\frac{K^{(1)}}{P}\left[E\left(P,\frac{\pi}{4}-\frac{\gamma}{2}\right)-E\left(P,\frac{\pi}{4}\right)\right],\\
U_{\text{barbule}}^i &= \frac{1}{2}\frac{D^{(2)}}{l^{(2)}}\int_0^1 \left(\frac{\mathrm{d}\theta}{\mathrm{d}\bar{s}}\right)^2 \mathrm{d}\bar{s} = 2\frac{D^{(2)}}{l^{(2)}}\cdot\frac{K^{(2)}}{p_i}\left[E\left(p_i,\frac{\beta_i+\Theta_i}{2}+\frac{\pi}{4}\right)\right.\\
&\quad \left.-E\left(p_i,\frac{\alpha_0^{\text{barbule}}+\alpha_i+\Theta_i}{2}+\frac{\pi}{4}\right)\right],\\
U_{\text{spring}}^i &= \frac{1}{2}\frac{D^{(2)}}{l^{(2)}}\bar{\lambda}\alpha_i^2,
\end{aligned} \tag{28}$$

Furthermore, substituting the above three strain energy components into Eqs. (26) and (27), the dimensionless total strain energies of the LargeRM and LargeNRM are finally obtained as

$$\begin{aligned}
\bar{U}_{\text{LargeRM}}^k &= \frac{l^{(1)}U_{\text{LargeRM}}^k}{D^{(1)}} = 2\left(\frac{K^{(1)}}{P}\left[E\left(P,\frac{\pi}{4}-\frac{\gamma}{2}\right)-E\left(P,\frac{\pi}{4}\right)\right]\right.\\
&\quad +\frac{D^{(2)}}{D^{(1)}}\cdot\frac{l^{(1)}}{l^{(2)}}\sum_{i=1}^k\left(\frac{K^{(2)}}{p_i}\left[E\left(p_i,\frac{\beta_i+\Theta_i}{2}+\frac{\pi}{4}\right)\right.\right.\\
&\quad \left.\left.\left.-E\left(p_i,\frac{\alpha_0^{\text{barbule}}+\alpha_i+\Theta_i}{2}+\frac{\pi}{4}\right)\right]+\frac{1}{4}\bar{\lambda}\alpha_i^2\right)\right),\\
\bar{U}_{\text{LargeNRM}}^k &= \frac{l^{(1)}U_{\text{LargeNRM}}^k}{D^{(1)}} = 2\left(\frac{K^{(1)}}{P}\left[E\left(P,\frac{\pi}{4}-\frac{\gamma}{2}\right)-E\left(P,\frac{\pi}{4}\right)\right]\right.
\end{aligned} \tag{29}$$

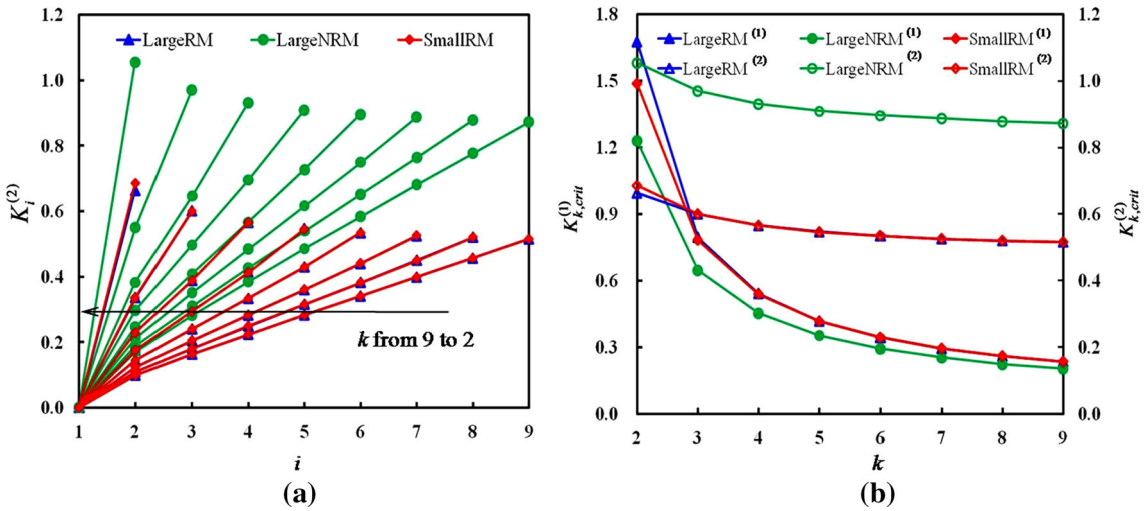

Fig. 4 Comparison of interlocking forces in the interlocking barbules, and critical forces of the barbs and barbules in eight critical states between LargeRM (blue lines), LargeNRM (green lines), and SmallRM (red lines, [2]). **a** Comparison of interlocking forces in the un-detached barbules. **b** Comparison of the critical forces of the barbs and barbules. Note the superscripts (1) and (2) in the legends indicate the barb and barbule, respectively (color figure online)

$$+\frac{D^{(2)}}{D^{(1)}}\cdot\frac{l^{(1)}}{l^{(2)}}\sum_{i=1}^{k}\left(\frac{K^{(2)}}{p_i}\left[E\left(p_i,\frac{\beta_i+\Theta_i}{2}+\frac{\pi}{4}\right)\right.\right.$$
$$\left.\left.-E\left(p_i,\frac{\alpha_0^{\text{barbule}}+\Theta_i}{2}+\frac{\pi}{4}\right)\right]\right), \tag{30}$$

5 Results and discussion

On the basis of the LargeRM and LargeNRM, dimensionless parameters ($\alpha_0^{\text{barbule}} = 30°$, $\psi_{frict} = 45°$, $L^{(2)}/l^{(2)} = 1.2$, $l^{(1)}/l^{(2)} = 10$, and $\Lambda = 1.0$ in the LargeRM) were first selected to study the eight critical detaching states in the delaminating process of the two neighboring barbs in Fig. 3a. Meanwhile, to neglect the influence of the barbule, $D^{(2)}/(l^{(2)})^2 << D^{(1)}/(l^{(1)})^2$ should be held, e.g., $D^{(2)}/D^{(1)} << (l^{(2)}/l^{(1)})^2 = 0.01$, and $D^{(2)}/D^{(1)} = 0.001$ was here used to calculate the dimensionless strain energies of the two models in Eqs. (29) and (30). Here, the SmallRM in [2], where the small-deformation barb was treated, was also included to be compared with the present models. For critical detaching states of the kth pair of interlocking barbules, the interlocking forces $K_i^{(2)}$ ($i \le k$) of the un-detached barbules, the critical force $K_{k,crit}^{(2)}$ of the barbules, and the corresponding critical detaching forces $K_{k,crit}^{(1)}$ of the barbs for the LargeRM (blue lines), LargeNRM (green lines), and SmallRM (red lines [2]) models are plotted in Fig. 4.

Figure 4a shows the interlocking forces of the barbules ($1 \le i \le k$) in all three models. It is worth mentioning that the interlocking force of the first pair of barbules is always 0 (i.e., $i = 1$), and this results from its location at the fixed end of the barb, and the barb deformation does not cause its deformation, whereas the interlocking forces of the barbules ($1 < i \le k$) in the LargeRM and LargeNRM are linearly distributed, which is the same as that of the SmallRM in [2], where the small-deformation barb was treated. This illustrates that the change of the small-deformation barb in the SmallRM to large-deformation barb in the LargeRM and LargeNRM does not change the distribution style of the interlocking force. Moreover, the interlocking force of the barbules in the non-rotatable LargeNRM is greater than those of the rotatable SmallRM and LargeRM. The interlocking forces of the SmallRM are slightly greater than those of the LargeRM, and this is attributed to the over-estimation of the small-deformation barb in SmallRM. Figure 4b shows the critical forces $K_{k,crit}^{(2)}$ of the barbule, which share the order of the interlocking force in Fig. 4a, i.e., LargeNRM > SmallRM > LargeRM. This can be explained by the absence of the rotatable joint in the LargeNRM, which enables a greater deformation of barbules during the delamination. However, the critical force $K_{k,crit}^{(1)}$ of the barbs is in

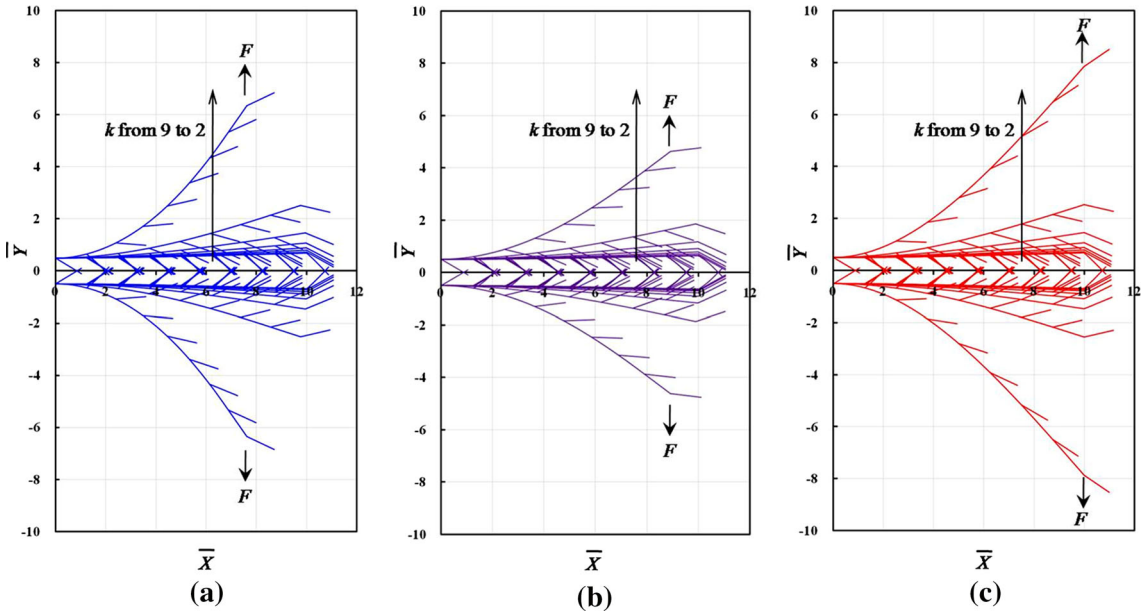

Fig. 5 Rupture profiles of the eight critical states of the barb–barbule structure in **a** LargeRM, **b** LargeNRM, and **c** SmallRM [2]

the inverse order, i.e., LargeRM > SmallRM > LargeNRM, and this is also due to the presence of the rotatable joint, which requires a greater force to produce a greater deformation of the barbs delaminating the barbs. The detaching force gradually increases when k changes from 9 to 2; in particular, the force increases sharply when k is from 3 to 2. This is because the interlocking barbule is close to the fixed end of the barb, and the constricted barbs improve the detaching force of the second pair of interlocking barbules. Interestingly, when k varies from 9 to 2, $K^{(1)}_{k,crit}$ increases 6–9 times, while $K^{(2)}_{k,crit}$ increases less than 1.5 times. This indicates the flaw-tolerant application with reduced number of barbules [2], which finitely influences the detaching forces and further improves the feather robustness. In other words, if there are some absent (or detached) barbules near the free end of the barb, they will produce weak influence on the delamination of the feather.

Figure 5 shows the profiles of the eight critical delamination states of the three models. It is noted that the dimensionless coordinates of the barbs (Eq. (16)) are normalized by the barbs' length $l^{(1)}$, whereas the coordinates of the barbules (Eqs. (22), (24), and (25)) are normalized by deformed barbules length $l^{(2)}$. Thus, the coordinates of the barbs were multiplied by $l^{(1)}/l^{(2)}$ to unify their profiles in a same coordinate system. The profile shows that the critical deformation in the LargeRM (Fig. 5a) is greater than that in the LargeNRM (Fig. 5b) due to the rotatable joint. In particular, when $k = 2$, the large-deformation barb (LargeRM, Fig. 5a) is different from the over-estimated small-deformation barb (SmallRM, Fig. 5c), whereas the critical deformations of the barbs in the three models are slightly different when $k \geq 4$. Figures 4 and 5 show that the rotatable joint in LargeRM/SmallRM strongly influences the behavior of the feather.

Addressing why the barbule rotation occurs in the delaminated barbs, we here give an insight from the viewpoint of the rotation toughening mechanism. Figures 6a–c show the elastic strain energies of different components in the three barb–barbule models. It is seen that when k is small, the elastic strain energies of the barbule and angular spring are much smaller than that of the barb due to the weak materials property of barbule. The strain energies of the barbule in the rotatable model (LargeRM and SmallRM) are less than those in the non-rotatable model (LargeNRM). However, the total elastic strain energies in the rotatable LargeRM and SmallRM are greater than those in the non-rotatable LargeNRM, see Fig. 6d. Plus, the total elastic stran energies of the rotatable models (LargeRM and SmallRM) are twice more than that of the non-rotatable one (LargeNRM) when the barbs are completely detached (i.e., when $k = 2$), and the total elastic strain energy of the rotatable SmallRM is 1.3 times that of LargeRM. This suggests that in the delamination of two neighboring barbs, the function of the rotatable joint is to increase the deformation of barb to store more elastic strain energy of the barb–barbule system instead of storing the energy in the rotatable barb–barbule joint and barbule. Also, the rotatable barb–barbule models are tougher than the non-rotatable; in other words, to delaminate the two neighboring barbs, greater force needs to be applied, and this results in more energy stored in the rotatable models. For example, considering $D^{(1)} = 0.5\ \mathrm{N}\cdot\mathrm{mm}^2$ and $l^{(1)} = 10$ mm, the energies in the three models

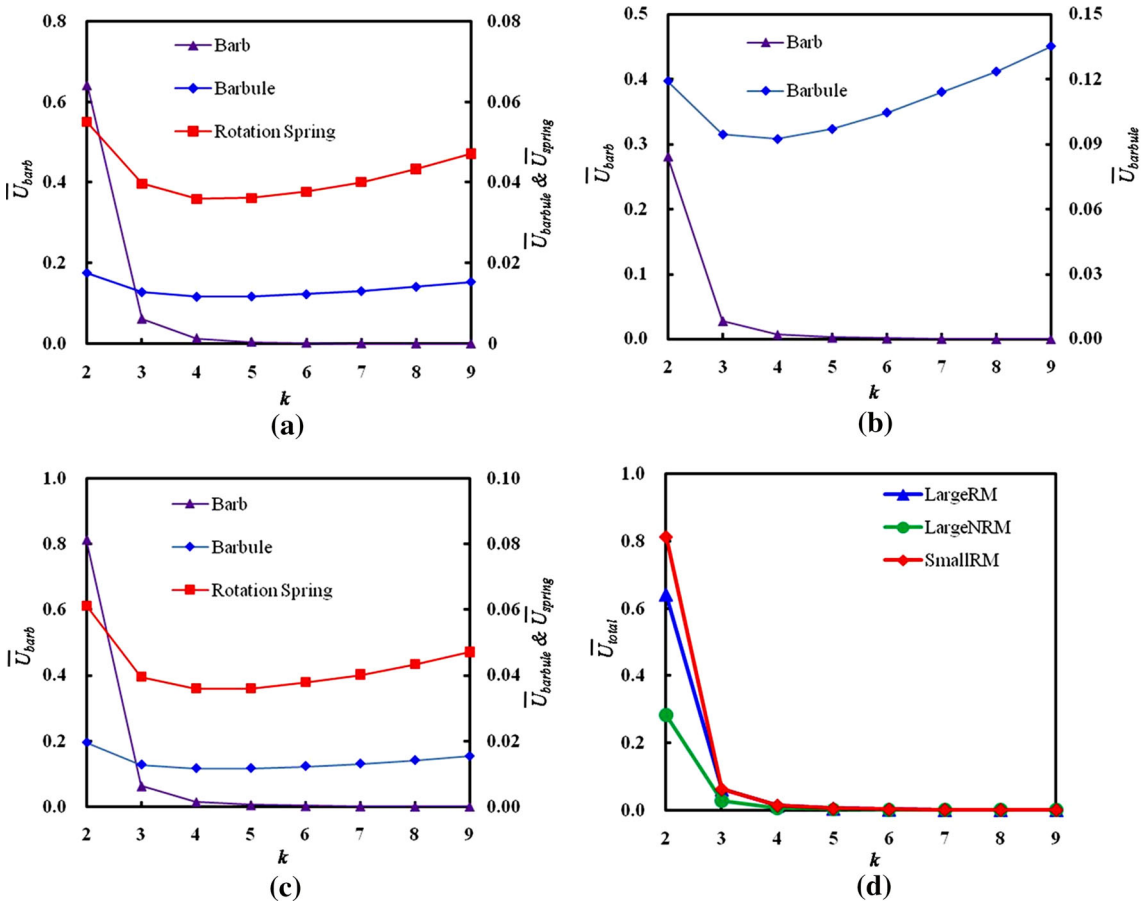

Fig. 6 Elastic energies of the three components in the **a** LargeRM, **b** LargeNRM, **c** SmallRM, and **d** comparison of total energies of the three barb–barbule models

are in the order of SmallRM (41 mJ) > LargeRM (32 mJ) > LargeNRM (14 mJ) when the second pair of the barbules detached. As mentioned before, compared to the LargeNM, the slight greatness of the SmallRM is due to the over-estimated small-deformation barb. Interestingly, the total elastic energy is not much changed when k decreased from 9 to 4, and this again exhibits the flaw or damage tolerance when finite interlocking barbules are detached.

Figure 7 shows the plot of the force–displacement curves of the three models, and due to the weak barbules, the detaching process includes eight load jumps (e.g., the jumps indicated by dash arrows for $k = 2$ in the three models). The SmallRM is a line (red) due to the small-deformation barb. After the detachment of the last pair ($k = 2$) of interlocking barbules, the LargeRM (blue) and LargeNRM (green) coincide with each other because of the absence of the interlocking barbules. Similarly, when $k \geq 4$, they show weak difference between the three models. Moreover, the last pair ($k = 2$) of barbules in the LargeNRM detaches ahead of the LargeRM and SmallRM because its barbules do not rotate. In particular, when $k = 3$, the displacement and force are 2 mm and 3 mN, respectively, and this is comparable to those in [1] for the swan (*Cygnus olor*), which are about 3.5 mm and 3 mN, respectively. In this aspect, the two simplifications in the present model are reasonable, and the model is applicable.

The friction-based detaching criterion in the present work is useful. It explores the nonlinear mechanical behavior of the basic barb–barbule structure in feathers and explains the importance of the rotatable barb–barbule joint to improve the structural toughness as well. Not only this, the friction-based criterion could be transferred to other-based structures, e.g., adhesion-based structure. In this regard, when the critical adhesion index is approached, the detachment occurs. Besides, the present nonlinear theory could be used to guide the design of new interlocking materials, such as the nature-inspired Velcro fastener [20,21]. For instance, the normal detaching behavior and shearing stick-slip frictional dynamics of the Velcro fasteners were experimentally studied [22,23], and they showed that because of the hook's nonlinear hyper-elastic deformation, the

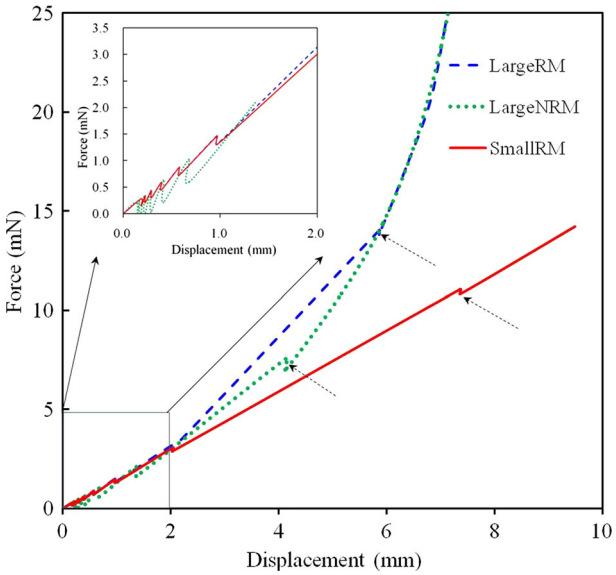

Fig. 7 Delamination of the three barb–barbule models. The dash arrows indicate the load jumps due to the detachment of barbules; the inset shows the load jumps of the detachments of the first several pairs of barbules

detaching mechanical properties are highly improved with respect to conventional Velcro materials. Of course, we admit that the present model is simplified because of the unilateral influence of the barb on barbule, but it still gives us a sight to understand the rotation function of the barb–barbule joint to improve the toughness of feather. Moreover, due to the absence of the experimental data, the validation is not fully presented even though the predicated value is comparable to that of the swan feather [1]. In the future, a numerical analysis of the barb–barbule interaction will be used to validate the theoretical model by given constitutive properties for bird feather types from the literature.

6 Conclusions

To explain the toughening mechanism of the rotation barb–barbule joint, a nonlinear mechanics of the barb-barbule substructure in feather was developed. The results of the rotatable LargeRM and non-rotatable LargeNRM showed that in the delamination, the interlocking force of un-detached barbules in both models was linearly distributed. Due to the rotation effect of the barb–barbule joint, the critical detaching force and the total elastic strain energy of the barb–barbule structure in the LargeRM are greater than those in the LargeNRM, and the function of the rotatable joint is to increase the deformation of the barb to store more energy instead of storing energy in the joint. Moreover, finite absent barbules did not much influence the total elastic strain energy of the barb–barbule structure, and this showed the flaw-tolerant ability. The present model reveals the delaminating mechanical behavior of two neighboring barbs in feathers and explains the function of the rotatable barb–barbule joint to increase the toughness of feather and further could be used to design new bio-inspired interlocking materials.

Acknowledgements This work was partially supported by the National Natural Science Foundation of China (NSFC) (Nos. 31300780, 11972118, 11772093, 61821002), the Fundamental Research Funds for the Central Universities (No. 2242016R30014, 2242017K40221), and ARC (FT140101152). NMP is supported by the European Commission with the Graphene Flagship Core 2 n. 785219 (WP14 “Composites”) and FET Proactive “Neurofibres” n. 732344 as well as by the MIUR with the “Departments of Excellence” grant L. 232/2016, ARS01-01384-PROSCAN and PRIN-20177TTP3S.

References

1. Kovalev, A., et al.: Unzipping bird feathers. J. R. Soc. Interface **11**, 20130988 (2014)
2. Chen, Q., et al.: An analytical hierarchical model explaining the robustness and flaw-tolerance of the interlocking barb-barbule structure of bird feathers. EPL **116**(2), 24001 (2016)
3. Chen, Q., Pugno, N.M.: Bio-mimetic mechanisms of natural hierarchical materials: a review. J. Mech. Behav. Biomed. Mater. **19**, 3–33 (2013)
4. Katti, K.S., et al.: Platelet interlocks are the key to toughness and strength in nacre. J. Mater. Res. **20**, 1097–1100 (2005)
5. Zhang, X., et al.: The beetle elytron plate: a lightweight, high-strength and buffering functional-structural bionic material. Sci. Rep. **7**(1), 4440 (2017)
6. Ennos, A., et al.: Functional morphology of the vanes of the flight feathers of the pigeon Columba livia. J. Exp. Biol. **198**(5), 1219–1228 (1995)
7. Worcester, S.E.: The scaling of the size and stiffness of primary flight feathers. J. Zool. **239**(3), 609–624 (1996)
8. Wang, X., et al.: Size scaling and stiffness of avian primary feathers: implications for the flight of Mesozoic birds. J. Evol. Biol. **25**(3), 547–555 (2012)
9. Purslow, P.P., et al.: Mechanical properties of primary feathers from the pigeon. J. Exp. Biol. **73**, 251–260 (1978)
10. Pennycuick, C.J., Lock, A.: Elastic energy storage in primary feather shafts. J. Exp. Biol. **64**, 677–689 (1976)
11. Lingham-Soliar, T.: Feather structure, biomechanics and biomimetics: the incredible lightness of being. J. Ornithol. **155**, 323–336 (2014)
12. Bonser, R.H.C., Purslow, P.P.: The Young's modulus of feather keratin. J. Exp. Biol. **198**, 1029–1033 (1995)
13. Wang, B., Meyers, M.A.: Light like a feather: a fibrous natural composite with a shape changing from round to square. Adv. Sci. **4**(3), 1600360 (2017)
14. Macleod, G.D.: Mechanical properties of contour feathers. J. Exp. Biol. **87**, 65–71 (1980)
15. Corning, W.R., Biewener, A.A.: In vivo strains in pigeon flight feather shafts: implications for structural design. J. Exp. Biol. **201**, 3057–3065 (1998)
16. Wang, B., et al.: Seagull feather shaft: correlation between structure and mechanical response. Acta Biomater. **48**, 270–288 (2017)
17. Chen, H., et al.: Biomimetic drag reduction study on herringbone riblets of bird feather. J. Bionic Eng. **10**, 341–349 (2013)
18. Sullivan, T.N., et al.: A lightweight, biological structure with tailored stiffness: The feather vane. Acta Biomater. **41**, 27–39 (2016)
19. Sullivan, T.N., et al.: Reversible attachment with tailored permeability: the feather vane and bioinspired designs. Adv. Fun. Mater. **27**(39), 1702954 (2017)
20. Pugno, N.M.: Velcro® nonlinear mechanics. Appl. Phys. Lett. **90**, 121918 (2007)
21. Chen, Q., et al.: Mechanics of plant fruit hooks. J. R. Soc. Interface **10**, 20120913 (2013)
22. Vokoun, D., et al.: Velcro-like fasteners based on NiTi micro-hook arrays. Smart Mater. Struct. **20**, 085027 (2011)
23. Mariani, L.M., et al.: Observations of stick-slip friction in Velcro®. Tribol. Lett. **56**, 189–196 (2014)

Supporting Materials

An energy-based study revealing the rotation toughening mechanism of barb-barbule joint in the barb delamination of feathers

Qiang Chen[1,*], Nicola Pugno[2,3,4], Zhiyong Li[1,5]

[1]*Biomechanics Laboratory, School of Biological Science &Medical Engineering, Southeast University, Nanjing210096, P.R. China.*

[2]*Laboratory of Bio-Inspired & Graphene Nanomechanics, Department of Civil, Environmental and Mechanical Engineering, University of Trento, I-38123 Trento, Italy.*

[3]*School of Engineering and Materials Science, Queen Mary University of London, Mile End Road E14NS, London, UK*

[4]*Ket Lab, Edoardo Amaldi Foundation, Via del Politecnico snc, I-00133 Rome*

[5]*School of Chemistry, Physics and Mechanical Engineering, Queensland University of Technology (QUT), Brisbane, QLD 4001, Australia*

By combining equations (8) and (11) in the paper, the equation system with unknown parameters α and β can be solved numerically with a given dimensionless force K. Moreover, the displacement components of the free end are calculated as:

$$\bar{\delta}_x = \bar{x}(\beta) - \cos\alpha_0 \tag{S1a}$$

$$\bar{\delta}_y = \bar{y}(\beta) - \sin\alpha_0 \tag{S1b}$$

Apparently, the displacement component in the x-direction (S1a) is negative. Addressing the solutions of the rotational cantilever, three cases sharing an angle φ=60°, are exemplified to discuss the influences of the included angle α_0, the materials property $\bar{\lambda}$, the force K. The three

cases are: (1) Case 1, α_0=45°, 90°, 135°, $\bar{\lambda}$ =1.0, and *K*=0.9; (2) Case 2, α_0=45°, $\bar{\lambda}$ =0.5, 1.0, 1.5, and *K*=0.9; (3) Case 3, α_0=45°, $\bar{\lambda}$ =1.0, and *K*=0.3, 0.6, 0.9. For the cases, their deformed profiles are plotted in Figure S1. The results can be easily understood, for instance, a greater materials property $\bar{\lambda}$ (or the greater rotation resistance) results in a smaller rotation deformation (Figure 2b); a greater force *K* results in a larger deformation (Figure S1c).

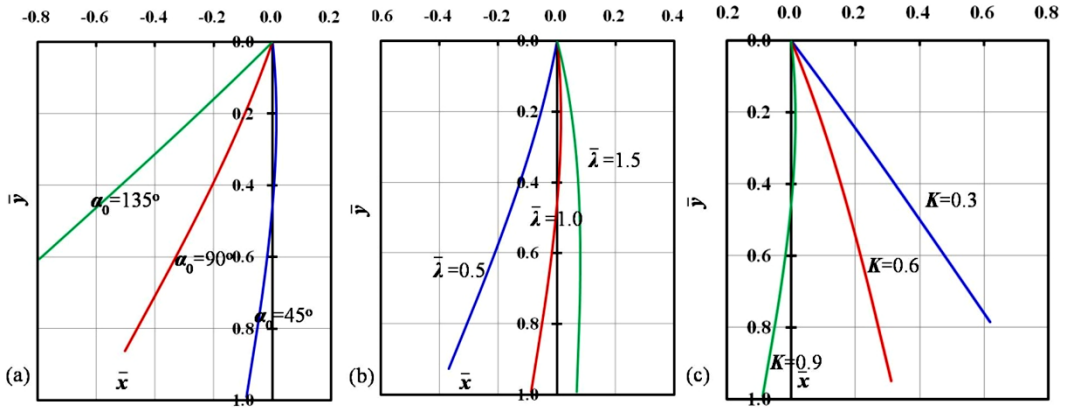

Figure S1. Deformed profiles of cantilevers under: (a) Case 1, (b) Case 2, (c) Case 3.

Moreover, the displacement components of the free end influenced by the three parameters are plotted in Figure S2. In general, the magnitude of $\bar{\delta}_x$ is greater than that of $\bar{\delta}_y$, and this is because the initial included angle α_0 locates between 45° and 135°, which results in a greater rigid rotation with respect the origin *O* and deformation in the *x* direction.

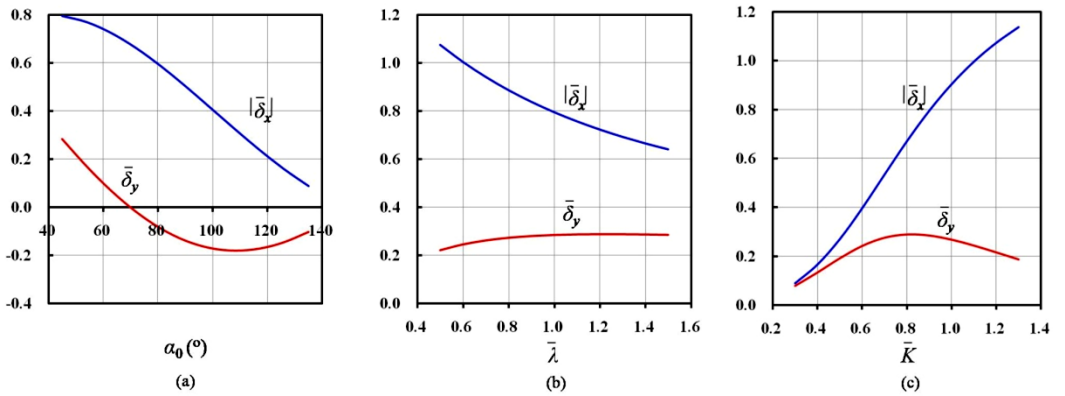

Figure S2. Displacement components of the free end of the cantilever influenced by: (a) Initial included angle α_0, (b) Materials parameter $\bar{\lambda}$, (c) Dimensionless force *K*.